High Momentum Jet Flames at Elevated Pressure: Detailed Investigation of Flame Stabilization with Simultaneous PIV and OH-LIF

Michael Severin*, Oliver Lammel, Holger Ax, Rainer Lückerath, Wolfgang Meier, Manfred Aigner
German Aerospace Center (DLR),
Institute of Combustion Technology,
Pfaffenwaldring 38-40, D-70569 Stuttgart, Germany

Johannes Heinze
German Aerospace Center (DLR),
Institute of Propulsion Technology,
Linder Höhe, D-51147 Köln, Germany

ABSTRACT

A model FLOX® combustor, featuring a single high momentum premixed jet flame, has been investigated using laser diagnostics in an optically accessible combustion chamber at a pressure of 8 bar. The model combustor was designed as a large single eccentric nozzle main burner (Ø 40 mm) together with an adjoining pilot burner and was operated with natural gas.

To gain insight into the flame stabilization mechanisms with and without piloting, simultaneous Particle Image Velocimetry (PIV) and OH Laser Induced Fluorescence (LIF) measurements have been performed at numerous two-dimensional sections of the flame. Additional OH-LIF measurements without PIV-particles were analyzed quantitatively resulting in absolute OH concentrations and temperature fields.

The flow field looks rather similar for both the unpiloted and the piloted case, featuring a large recirculation zone next to the high momentum jet. However, flame shape and position change drastically. For the unpiloted case, the flame is lifted, widely distributed and isolated flame kernels are found at the flame root in the vicinity of small scale vortices. For the piloted flame, on the other hand, both pilot and main flame are attached to the burner base plate, and flame stabilization seems to take place on much smaller spatial scales with a connected flame front and no isolated flame kernels.

The single shot analysis gives rise to the assumption that for the unpiloted case small scale vortices act like the pilot burner flow in the opposed case and constantly impinge and ignite the high momentum jet at its root.

Keywords: *high momentum jet flame, confined jet flame, jet flame stabilization, FLOX®, gas turbine combustion, high pressure test rig, laser diagnostics, PIV, quantitative OH-LIF, simultaneous, validation data set*

1 Introduction

High momentum jet stabilized combustion systems provide an interesting alternative for gas turbines, replacing state of the art swirl stabilized combustors. These high momentum jet combustion systems, also termed FLOX®-combustors [1, 2], have been shown to operate reliable, load- and fuel-flexible with low pollutant emissions in a wide range of gas turbine relevant conditions [3–6]. Note that the term FLOX® (flameless oxidation) is used for historical reasons and only refers to the kind of combustor and not to the kind of combustion (which is typically not "flameless" at gas turbine conditions).

A FLOX® burner consists of nozzles arranged in a circle, which feed a mixture of air and fuel into the combustion chamber at high flow velocities. The turbulent high speed pipe flow inside these nozzles provides sufficient premixing and high flashback resistance at a wide range of operation conditions and fuels. Previous research demonstrated operation with pure hydrogen is possible at gas turbine relevant conditions with low NO_x emissions and without flashback [7, 8]. A key feature of a FLOX® burner is the large inner recirculation zone, which brings hot burnt gas back to the combustor nozzles,

*Corresponding author: michael.severin@dlr.de

where it supports the ignition of the incoming high momentum jet of fresh unburned fuel/air mixture. However, the processes of mixing, ignition and flame stabilization in these kinds of combustors is not fully understood yet.

The circular arrangement of nozzles, with the corresponding strong density gradients within the combustion chamber, and the highly turbulent distributed combustion make it challenging for combustion diagnostics to gain insight into the detailed processes within a FLOX® combustion chamber [7]. Numerical simulations also struggle with the high Reynolds number flows, large shear rates, and distributed combustion [9, 10]. Thus model combustors, which are simplified and only represent a part of an actual FLOX® combustor, were used in the past to both experimentally and numerically investigate the features of high momentum jet flames.

The simplest model combustor is a lab-scale single nozzle burner, that has extensively been investigated at atmospheric conditions, both experimentally [11, 12] and numerically [13]. Furthermore, a 3-nozzle model combustor has been investigated at high pressure [8]. All of these model combustors were down-scaled compared to full size gas turbine combustors, and therefore it was challenging to perform measurements with sufficient spatial resolution in order to resolve structures in context of flame stabilization.

For the present work, a full-scale single nozzle burner was designed, so that a section of the actual gas turbine burner system could be investigated at relevant operating conditions. This includes, for example, real size fuel injectors and an unscaled mixing length, to represent the correct level of premixedness. Also, the length of the combustion chamber is designed to provide a realistic residence time within the combustor. These features are necessary for real scale chemistry. The motivation, design and characterization of this model burner, as well as the analysis of its load- and fuel-flexibility have been shown in the preceding ASME paper GT2017-64615 [14]. For the present study, two reference operation points for one injector/mixing configuration (CJ02GAS1) have been extracted from this basic characterization and investigated in detail with laser diagnostics, to gain insight into flame stabilization mechanisms.

2 Experimental Setup

The experiments were conducted at the high pressure test rig HBK-S at DLR Stuttgart, that enables the operation of the model burner under gas turbine relevant conditions. A key feature of the test rig is a large optical access from all four sides, which allows for the extensive application of laser based and other optical diagnostic measurements. A detailed description of this test rig is given in the preceding paper [14] and in previous publications [8].

A test carrier containing the plenum, the model combustor, the combustion chamber, and the exhaust gas nozzle was placed inside the pressure housing. The test carrier was equipped with numerous thermocouples, several static and dynamic pressure sensors, and an exhaust gas analysis probe at the end of the combustion chamber. The flame could be monitored via several surveillance cameras and chemiluminescence cameras. With these basic measurements, the model burner was characterized in its whole operational range, and reference operation points could be identified [14] for more detailed measurements, which is the scope of this contribution.

2.1 Model Combustor

Main part of the combustor is the long duct that represents a single FLOX® nozzle, where fuel and air mix and are fed to the combustion chamber (without swirl).

The preheated combustion air is guided from the plenum into the duct via an S-turn, to mimic the configuration in the real gas turbine combustor (where the air enters the combustor in an 180° turn). At the beginning of the duct, the fuel (natural gas) is added to the air flow by the exchangeable fuel injector GAS1, 400 mm upstream of the burner base plate. This air guidance and mixing section is not shown here, but can be found in detail in Figure 1 of the preceding paper [14].

The combustion chamber and the combustor head are shown in a schematic drawing in Fig. 1, where the end of the long mixing duct can be seen at the very left. The mixing duct has a diameter of 40 mm and is off-centered to the combustion

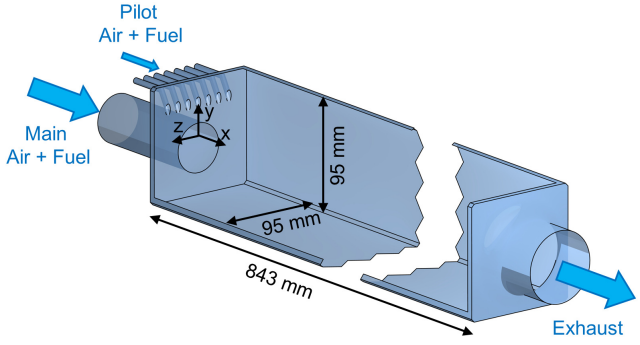

Fig. 1. Model combustor with dimensions and used coordinate system

chamber axis by 10 mm. Thus, the fuel/air mixture enters the combustion chamber as an off-centered partially premixed turbulent jet flow. This off-centered setup allows for the establishment of a distinct recirculation zone of hot burned exhaust gas at the top side of the combustion chamber. In addition, a model pilot burner is added to the burner base plate (see Fig. 1), that supports flame stabilization at the recirculation side of the jet. The pilot burner consists of 7 small pipes, arranged in a line and inclined at an angle of 60° towards the main jet axis. Like the main burner, the pilot pipes feed a preheated air/fuel mixture into the combustion chamber, typically with an equivalence ratio closer to stoichiometry. This setup of main and pilot burner is designed to recreate a sector of a full-scale gas turbine FLOX® combustor (c.f. [14]).

The combustion chamber has a quadratic cross section of $95 \times 95\,\mathrm{mm}^2$ and a length of 843 mm. It is optically accessible by all four sides through quartz glass window segments of size $160 \times 90\,\mathrm{mm}^2$, allowing for the extensive application of laser diagnostic methods. Some of the window segments in the rear part of the combustion chamber are replaced by instrumentation plates, holding pressure sensors and the exhaust gas probe. The exhaust gas nozzle at the end of the combustion chamber is centered and has a diameter of 58.8 mm.

Figure 1 also displays the used coordinate system: The axial direction is defined as x-axis, the vertical direction is y, and z is the lateral direction in which the combustor is symmetric. The origin is at the burner base plate for $x = 0$, and centered in the combustion chamber for x and y. This means the vertical symmetry plane is at $z = 0$ and the main nozzle axis is at $y = -10\,\mathrm{mm}$.

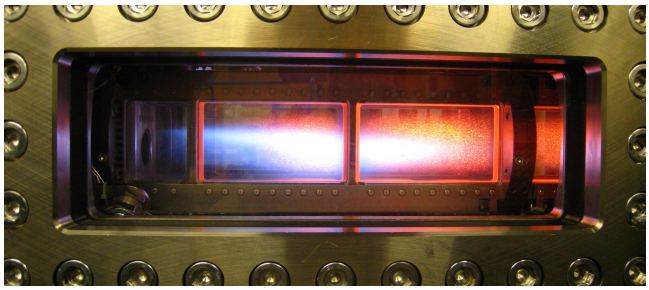

Fig. 2. Model combustor and optical combustion chamber in operation at the high pressure test rig HBK-S

2.2 Operation Conditions

For the analyses in this work, two operation points were chosen from the extensive parameter study presented in [14]: One reference case – termed U for unpiloted – with gas turbine typical parameters, except for a down-scaled pressure of 8 bars and one piloted case – termed P – where the pilot burner flame is added to the same main burner flame conditions. Both parameter sets can be found in detail in Tab. 1. In a real application, the pilot burner would be added to a leaner main flame to reach partload conditions where otherwise the unpiloted main flame could not be stabilized. For the sake of comparison and to gain insight on how the pilot burner changes flame stabilization, the main burner parameters are kept constant for both cases.

Table 1. Operating conditions overview

Case			U	P
Pressure	p	[bar]	8	8
Global air excess ratio	λ_g	[-]	1.83	1.70
Adiabatic flame temp.	T_ad	[K]	1900	1970
Main burner				
jet velocity	$v_\mathrm{jet,m}$	[m/s]	111	111
air excess ratio	λ_m	[-]	1.83	1.83
air preheat temp.	T_m	[K]	725	725
Pilot burner				
jet velocity	$v_\mathrm{jet,p}$	[m/s]	-	100
air excess ratio	λ_p	[-]	-	1.0
air preheat temp.	T_p	[K]	-	633

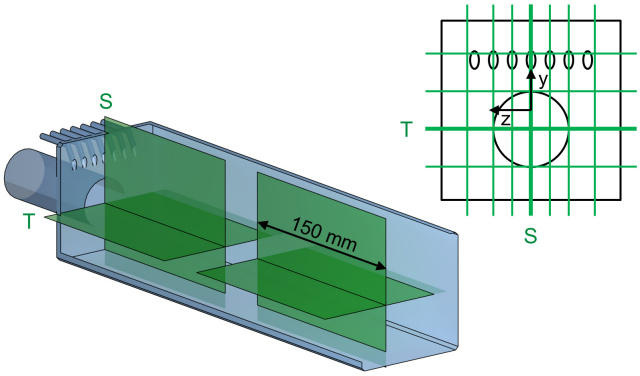

Fig. 3. Laser diagnostics measurement planes. Positions for orientation S (sideview): z = 0, ±10, ±20, ±33.8 mm. Positions for orientation T (topview): y = ±10, ±30 mm. Laser sheet extent in axial direction for the first and second window segment is x ≈ 5 - 150 mm and x ≈ 190 - 340 mm.

2.3 Measurement Planes

Optical measurements were performed in the first and second window segment (out of 5 segments in total). Note that the optical combustion chamber visible in Fig. 2 has been flipped in axial direction for the present measurements, so that the first two segments were both large windows of 160 mm length. A schematic drawing of the measurement locations can be found in Fig. 3. Planar measurements were done in x-y planes, denoted as orientation S (sideview), and in x-z planes, denoted as orientation T (topview). To change the orientation, the combustor head was rotated in the combustion chamber and the laser sheet always remained vertical.

The reference measurement planes are displayed in Fig. 3, intersecting at the nozzle axis at $z = 0$ mm and $y = -10$ mm. However, for both orientations and both window segments a scan was performed, resulting in 7 vertical and 4 horizontal planes. Their exact positions can be seen in the upper right of Fig. 3. If not denoted otherwise, the results shown in this work are always the reference planes S ($z = 0$ mm) and T ($y = -10$ mm).

Note that the identifiers S and T are also used for the OH*-CL images, although they are not planar measurements, but rather line-of-sight integrated information in z- (S) or y-direction (T).

2.4 Optical Measurement Techniques

OH* chemiluminescence (OH*-CL) was recorded in order to get information about the average flame shape and position, Particle Image Velocimetry (PIV) was applied to reveal the flow velocity field and planar OH Laser Induced Fluorescence (OH-LIF) was used to identify the interface between unburned and burned gas. All three measurement techniques were first used separately. Additional simultaneous PIV and OH-LIF measurements were acquired subsequently.

2.4.1 OH* Chemiluminescence

OH radicals in the electronically excited state (OH*) are formed by chemical reactions in the reaction zone, predominantly via CH + O_2 $\longleftrightarrow$ CO + OH* in hydrocarbon combustion [15]. The chemiluminescence emission of OH* is a spontaneous emission and can be imaged directly with a camera, usually equipped with an image intensifier and an appropriate filter. The signal intensity depends mainly on the concentration of OH*. OH* is only formed within the flame front and has a short lifetime. Thus, OH*-CL provides a good qualitative indication of the position and shape of the heat release zone. However, the emission detection is line-of-sight integrated and therefore the spatial resolution is compromised and the results are not directly comparable to planar methods (e.g. planar PIV and planar LIF).

The CL signal was imaged with an sCMOS camera (LaVision Imager sCMOS) equipped with an external image intensifier (LaVision IRO). The intensifier/camera system was equipped with a Halle UV quartz glass objective (focal length $f = 64$ mm) and a combination of interference filters (resulting in a transmission window at 310 ± 15 nm). The resulting field of view was 200×150 mm with a spatial resolution (in-plane) of less than 0.2 mm, so that one window of the combustion chamber could be imaged at a time. For each operating condition and measurement position, 500 single instantaneous images were recorded with a frame rate of 10 Hz. These images were processed by subtracting a background image and dividing them by the sensitivity distribution of the intensifier. The average of such an image series then reveals the characteristic flame shape without instantaneous turbulent fluctuations. The standard deviation of the image series on the other hand reveals the areas of highest fluctuation. The color scales for the OH*-CL intensity (in arbitrary units) of the figures presented in this work are normalized to a global maximum denoted as 100 % here.

Additional high-speed OH*-CL recordings have been done for the investigated operation points in both orientations with a frame rate of 10 kHz and 10000 images per series. Results of these high-speed measurements are not shown in this

contribution since their evaluation is not finished yet. However, they may be valuable for the interpretation of the present results in terms of flame stabilization in the future.

2.4.2 Particle Image Velocimetry

Two-component velocity fields in several planar sections through the combustion chamber were measured using PIV. The PIV method determines local fluid velocities by analyzing the displacement of small seeding particles during a short time span. To measure this displacement, the particles are illuminated twice by a laser sheet with an appropriate separation time and imaged with a camera.

A twin head flashlamp-pumped Nd:YAG laser (Litron Nano L 200-15 PIV) was used for the generation of the two laser pulses ($\lambda = 532$ nm, pulse energy 2×200 mJ, pulse duration 5 ns). A set of (anti-reflective coated) cylindrical lenses and high-reflective mirrors converted the laser beam into a 150 mm wide laser sheet and guided it vertically into the combustion chamber. The sheet forming optics were used for both the PIV and the LIF laser beam (see next section) and were therefore double-coated with an anti-reflective / high-reflective layer for both laser wavelengths 532 nm and 283 nm. The thickness of the laser sheet within the combustion chamber was approximately 1 mm, which limits the spatial resolution in sheet-normal direction.

The two particle illuminations were imaged with a double-frame CCD camera (LaVision Imager Pro X), which was triggered synchronously with the laser pulses. The camera chip had an image resolution of 1600×1200 pixels. The camera was equipped with a standard Nikon lens (focal length 50 mm) covered with a narrow band interference filter (532 nm), reducing the influence of broadband light sources such as the flame. The resulting field of view was 160×120 mm, so that the whole laser sheet width and combustion chamber height could be imaged with a resolution of 10 px/mm.

An air flow seeded with titanium dioxide particles (nominal diameter 1 µm) was generated by a fluidized bed seeder and then fed into the main air flow. For the piloted flame, a second seeder was added and fed into the pilot air flow. The seeded air flow was only applied during the PIV measurements because it reduces window transmittance quickly. The recording rate of the PIV system was 10 double frames per second. The separation time between the two laser pulses was chosen between 4 µs and 6 µs, depending on the operating condition and measurement position.

The particle images were preprocessed to remove stationary patterns caused by light reflections or impurities on the windows. Velocity fields were determined from the preprocessed images using commercial software (LaVision DaVis 8.2). Instantaneous velocity fields were calculated using a multi-pass cross-correlation algorithm with a final circular interrogation window size of 12 pixel. Therefore the resulting spatial vector resolution was 1.2 mm in in-plane and 1.0 mm in plane-normal direction. The interrogation windows were placed with a 50 % overlap, which resulted in a final vector grid of $0.6 \times 0.6\,\text{mm}^2$ (the spatial resolution is unaltered by this overlap). The resulting vector fields were postprocessed in order to identify and remove erroneous vectors, which were partially replaced by interpolated vectors.

500 double images were recorded for each measurement and the resulting instantaneous vector fields were averaged to reveal the mean flow field without turbulent fluctuations and the standard deviation was derived to reveal the velocity fluctuation intensity. A minimum of 50 valid instantaneous vectors per position was defined to obtain a valid average and standard deviation. Since this number could not be reached in some corners of the measurement planes the final interrogation window size was increased to 32 px to get a valid and converged average everywhere. This of course sacrificed spatial resolution, which however, was still sufficient for the average velocity field since small scale structures are smoothed out there anyway (all the instantaneous velocity fields shown in this work are obtained with the 12 px interrogation window).

The PIV measurements are encumbered by the harsh conditions at the high pressure test rig. Temporal fluctuations of temperature and density in the combustion chamber degrade planeness and homogeneity of the laser sheet. As temperatures in the combustion chamber rise, the windows of the chamber have to sustain very high heat loads. The glass begins to soften and its surface becomes rough and increasingly opaque. Furthermore, during the PIV measurements the window staining was significantly increased by seeding particles adhering to the quartz glass. This is a major problem for the PIV technique because the stray light formed at the window surface has the same wavelength as the light scattered by the particles. The increasing stray light due to window staining leads to a continuously decreasing quality of the particle images. After a total of 5 minutes of seeded air flow (which corresponds to 3-5 measurements series) the stray light was too strong to allow further imaging of seed particles. The test rig was then shut down and the windows were cleaned or replaced.

Based on the ± 0.1 pixel uncertainty of the applied peak-finding algorithm, the random uncertainty of the two-component instantaneous velocities is ± 2.5 m/s.

2.4.3 OH-LIF and Thermometry

The concentration distribution of OH was measured by planar laser induced fluorescence (LIF). OH is an intermediate product formed in the reaction zones of hydrocarbon flames that persists in the exhaust gas as long as temperatures are high. It is therefore useful to distinguish burned from unburned fluid in combustion diagnostics.

Under realistic test conditions the high OH concentrations lead to laser absorption of up to 50 %. Thus simultaneous measurements of LIF and absorption were made to correct the LIF images for laser absorption on a single pulse basis. The

basic idea of the image post-processing is to use the simultaneous LIF and absorption measurements together for the absolute calibration of the OH concentration. The absorption is correlated directly with the integral number density of the probed OH quantum state along the way of the laser beam through the combustor, while the absorption corrected LIF image tells how to distribute the integral number of OH molecules along the laser beam. A detailed description of the algorithm is given in reference [16].

The OH equilibrium concentration in a lean flame ($\lambda \geq 1.1$) increases nearly exponentially with respect to temperature and is almost independent of equivalence ratio. At elevated pressures ($p > 5$ bar) the relaxation processes are fast enough to assume equilibrium concentration of OH. Thus, in lean high pressure flames, the OH concentration is a very sensitive temperature indicator and can directly be transformed into temperature in a range from 1400 K (sufficient OH-LIF) to 2600 K (reduced temperature sensitivity of the OH-LIF).

To excite the OH radical the wavelength of a pulsed, frequency doubled dye laser system (Sirah, Model PrecisionScan, 20 mJ/pulse, 8 ns pulse width), pumped by a Nd:YAG Laser (Spectra Physics, Model PIV 400-10, 10 Hz repetition rate), was tuned to an OH absorption line representing the total OH density, namely Q1(9.5)+Q2(7.5) [17] at 283.9 nm. For the OH concentration measurements under these experimental conditions, the excitation of this spectrally overlapping line pair is very attractive for several reasons (see [16]). The UV laser beam was combined with the PIV laser beam, before the beams reached the light sheet optics. So the UV laser light sheet was formed of same dimension and direction as the PIV sheet. Combining both laser beams ahead of the sheet forming optics simplifies the experimental setup and saves space which is limited at the high pressure test rig. However, this setup has the disadvantage that the sheets cannot be adjusted independently so that the sheet optimization (parallelism, focus,...) always is a compromise between both wavelengths. The thickness of the LIF laser sheet in the combustion chamber (and thus the sheet-normal spatial resolution) was approximately 0.5 mm. The spatial resolution in-plane of the laser sheet was the same as for OH*-CL, i.e. 0.2 mm.

The OH-LIF signal was spectrally filtered and detected by the same filter/intensifier/camera system that was used for OH*-CL. The only change was a reduced exposure gate time of 100 ns. A second intensified CCD camera measured the intensity distributions of both laser sheets before and behind the combustor by reflecting a small portion of the laser sheet into reference cells filled with appropriate dye solutions (Rhodamin 6G solved in Ethanol). To capture both reference cells with one camera, they had to be placed right next to each other. To determine the part of laser attenuation caused by the OH absorption on a single-image basis, each absorption image ("on-resonance" image) of the second camera was normalized to the equivalent time averaged image at which the laser frequency was detuned from the OH resonance ("off-resonance" image), taken just before or after the single pulse OH image series. Although the fluorescence intensities of the reference cells were sufficient, an image intensifier had to be used as well, in order to achieve the small exposure gate to capture the LIF laser pulse in the reference cells well separated from the PIV laser (which was guided into the cells as well due to the laser combination ahead of the sheet forming).

Corresponding to the PIV and CL measurements, 500 instantaneous LIF and absorption images were recorded for each measurement run. A "grid image" was taken each day, where a non-uniform grid was placed in the laser sheet which allowed to exactly map three laser sheet images of the LIF signal and the two reference cells onto each other.

The processing of the OH-LIF images to absolute concentration and to temperature fields followed the method by Heinze et al. [16] and will therefore be described only briefly here: First, the LIF image is corrected for the camera/intensifier background and sensitivity. Second, it is normalized to the incoming laser sheet energy (usual sheet correction). Third, from the absorption images the integral absorption is determined line by line as a profile across the laser sheet. The local laser energy distribution can easily be reconstructed, assuming a proportionality of OH-LIF and local absorption. This assumption is fulfilled in good approximation for the used OH B-X LIF transition [18]. Then, the sheet-corrected LIF image is divided by the local laser energy to account for the energy loss due to absorption. Multiplying the ratio of integral absorption to integral LIF signal, together with some thermodynamic quantum mechanical and geometric parameters (Einstein B coefficients, ground state population, etc.), the arbitrary LIF signal is calibrated to an absolute OH number density.

In a subsequent step, the OH concentration can be transformed into temperature (T) assuming local equilibrium conditions. Therefore a range of equilibrium calculations (equilibrium at various T and λ and constant pressure) is performed with the software GASEQ and the nominal mass flows and preheat temperatures for air and natural gas. The result is a function of OH depending on local T and local λ. Fortunately this function is nearly independent of equivalence ratio λ in lean premixed flames ($1.1 < \lambda < 3$), so that a mean mapping function $T(\mathrm{OH})$ can be derived and applied to the OH concentration results. The advantages of this temperature derivation are its simplicity and the strong sensitivity of OH from T (the concentration of OH approximately doubles each 100 K). The obvious drawback is that in colder regions and particularly in the incoming fresh gas, OH concentrations are so low or non-existent that no temperature can be derived there.

An error estimation for the derived temperatures has been conducted: Following Heinze et al. [16], the various measurement uncertainties add up to an error of ± 20 % in OH concentration. Because of the favorable nonlinear relation between OH and T, this results in an error of less than ± 3 % for temperatures around 2000 K. However, at lower temperatures this quasi-logarithmic relation leads to a sudden increase in temperature error, when random background noise appears in the same order of magnitude as the measured signal (stray light, intensifier noise, OH*-chemiluminescence, etc...). Furthermore, since both integral absorption and integral LIF signal approach zero in this low temperature region, their ratio becomes more

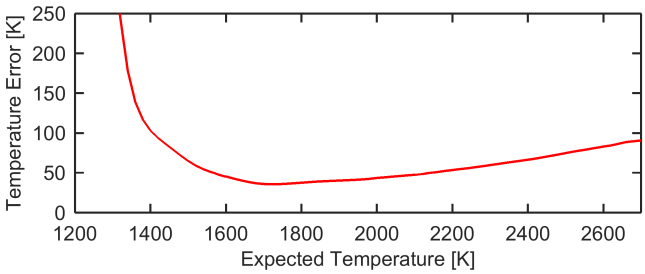

Fig. 4. Estimated OH-LIF temperature evaluation error

and more arbitrary. The result of this error estimation for the present hardware setup is given in Fig. 4. On this basis, the lower limit for the temperature evaluation has been set to 1400 K, where the error is barely acceptable at ± 100 K. In the presented experimental investigation, we believe the main reason for the background signal was stray light due to reflexions of the OH-LIF and OH*-CL radiation at the numerous quartz glass surfaces in the high-pressure test-rig (there are two layers of combustion chamber windows and one pressure window in each direction). This effect is hardly avoidable for high-pressure experiments, but could be minimized by the use of anti-reflective window coatings.

A further uncertainty is that the assumption of equilibrium is not valid in the vicinity of the flame front, where OH exists in superequilibrium concentration. However, in lean premixed flames at a pressure above 5 bar, superequilibrium OH relaxes within fractions of a millimeter [16]. This effect is not accounted for in Fig. 4.

Keeping these limitations in mind, the result as "T from equilibrium OH" can be seen as a much more intuitive quantity than an OH concentration. In an ongoing work, the results and the accuracy of this thermometry method will be compared to other laser temperature measurement techniques (CARS, Raman).

3 Results

The measurement results are split in three parts: First, the temporal averages of separate OH*-CL, PIV and OH-LIF measurements are displayed and related to each other for the main measurement planes. Second, this statistical information is expanded into a three-dimensional analysis of all measured planes. Last, the results of the simultaneous PIV / OH-LIF measurements are shown in exemplary single shots and analyzed.

For an easy assignment of the respective operation condition and measurement plane to the shown plots, the capital letters U or P (for the operation conditions unpiloted/piloted) and S or T (for measurement planes sideview/topview) are depicted in the top right corner of every plot.

3.1 Averaged Results

The flame shape and position can best be revealed qualitatively by the averaged OH*-CL images. These ensemble averages are shown in Fig. 5 for both the unpiloted and the piloted case, each of them in a side (x/y) and a top (x/z) view. Note that the OH*-CL results are no planar information, but line-of-sight integrated in image-normal direction. It is obvious that the flames look fundamentally different: The unpiloted flame is lifted from the burner base plate by a few centimeters and is widely distributed within the combustion chamber with a comparatively low OH*-CL intensity. The maximum average intensity is far downstream at approximately $x \approx 250$ mm. In contrast, the piloted flame is attached to the nozzle rim, with the maximum intensity close to the burner base plate right where the pilot jets impinge the main jet. It has a shorter flame length, and is more compact in y-direction. In z-direction, the extent of both flames is similar.

The corresponding average flow fields to these cases are shown in Fig. 6. The flow direction is shown by black streamlines, the velocity magnitude ($v_t = \sqrt{v_x^2 + v_y^2}$) is plotted as a colored background. A white line is drawn at $v_x = 0$ to show the extent of the recirculating regions of the flow. The expanding and decelerating high momentum jet is clearly visible in all four plots. For both cases U and P, a large recirculation zone can be seen in orientation S at the top side of the jet. The recirculation zone is a little shorter for case P but more bulgy. The jet in return seems to be slightly pushed down and constricted. The impinging pilot burner flow is visible at the top nozzle rim in view S of case P. Although it is not surprising that the pilot flow pushes down the main jet, it is noticeable that the effective change in the flow field is most pronounced far downstream around $x \approx 200$ mm. The penetration depth of the jet into the combustion chamber is very similar for both cases on the other hand. A tiny recirculation zone is visible on the bottom side of the jet for case U, but not for P. This was also verified for the planes $z = \pm 10$ mm, not shown here.

In orientation T, the lateral spreading of the jet is visible for both cases. However, for case P the spreading angle is much wider, which means the jet dodges the vertical constriction by broadening in z. Also the lateral recirculation zones visible for case U vanish almost completely for case P. For both cases, a slight asymmetry can be seen, which could be due to installation impurities and/or buoyancy effects.

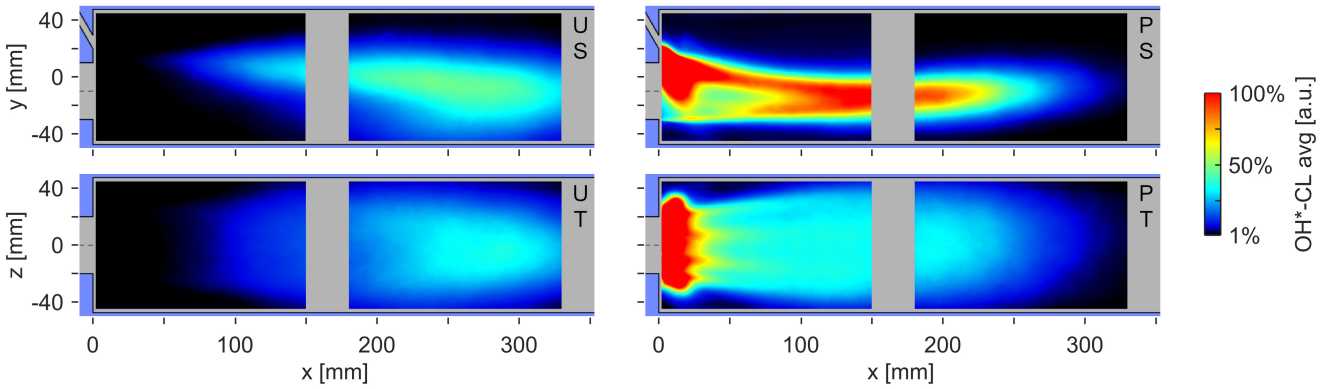

Fig. 5. OH*-CL average images, normalized to a common maximum. Left images show the unpiloted case (U), right images the piloted case (P). For each case, sideview (S) and topview (T) are shown. These abbreviations hold for all figures.

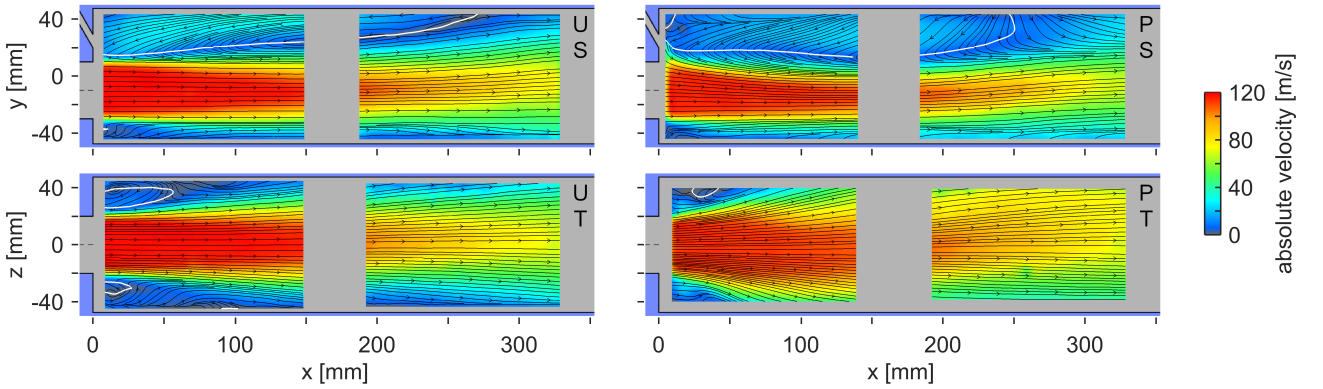

Fig. 6. PIV average streamlines and colored velocity magnitude. The white contour at $v_x = 0$ m/s shows recirculation zones.

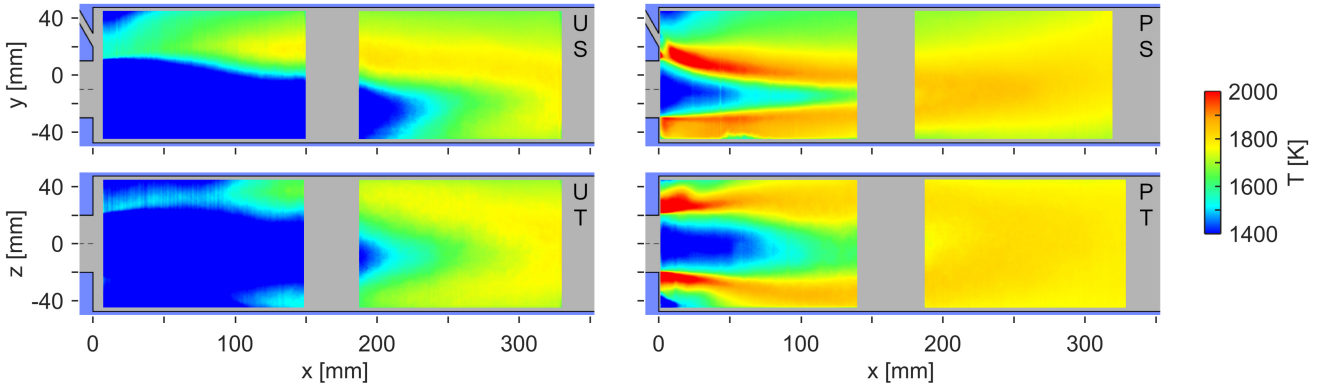

Fig. 7. Averaged temperature distributions from OH-LIF thermometry

In Fig. 7 the averaged temperature fields derived from the OH-LIF thermometry are shown. Note that the temperature evaluation has to be done on a single shot basis before the averaging, since the equilibrium correlation of OH vs. T is strongly non-linear. Another concern of the temperature averaging are the regions without OH, i.e. the unburned gas: From the intensifier noise, the evaluation results in arbitrary temperatures of $1000-1200$ K for these regions, which is considerably higher than the actual preheat temperature of the fresh gas. Therefore, the temperature average might be biased to higher temperatures for intermittent regions of burned and unburned gas.

For case U view S, maximum temperatures can be seen in the upper half of the combustion chamber, which matches the observation from the asymmetric OH*-CL image (U-S in Fig. 5), that the flame burns mostly at the top side of the jet. High temperature regions of roughly 1600 K reach back up to the burner base plate, which must be recirculated burned gas, since no reaction was visible in the OH*-CL images below $x \approx 50$ mm.

Table 2. Exhaust gas emission measurements

Case		U	P
NO_x @ 15 % O_2	[ppm]	2.5	9.0
CO @ 15 % O_2	[ppm]	4.2	7.0

Starting from the burner base plate, the interface between hot exhaust gas and cold fresh gas first follows the interface between jet and recirculation zone (white line in Fig. 6 U-S). At $x = 50$ mm, the temperature interface bends downwards, into the intermediate velocity regions of the spreading jet, which probably is a sign of entrainment of hot exhaust gas into the incoming fresh gas. Further downstream, at $x = 100$ mm, an increase in temperature can be seen and a band of maximum temperature is distributed from this upper shear layer towards the tip of the jet at the center line at $x \approx 330$ mm. This is the region where most of the reaction takes place, in agreement with the OH*-CL flame shape. No elevated temperatures can be seen at the bottom side of the jet up to $x \approx 100$ mm. This explains why no reaction can be seen at the bottom side of the jet, although the streamlines suggest a similar amount of entrainment: The entrained surrounding gas at the bottom side is too cold to initiate reaction. In the corresponding view U-T, again a slight asymmetry can be seen, but the temperature signal in the positive z side is hardly above detection threshold. Up to $x \approx 100$ mm temperatures are rather low, like on the bottom side.

Temperature distribution changes drastically for case P: The maximum temperatures are found close to the burner base plate, where the pilot impinges onto the main jet. Unlike the line-of-sight integrated OH*-CL images, the planar measurement can now resolve the penetration depth of the pilot burner: In the symmetry plane S, the pilot burner flame is mostly deflected by the main jet, and it is obvious that the pilot flame aligned with the pilot nozzles visible in Fig. 5 must be from the outer pilot nozzles. However, a slight penetration of the temperature interface into the main jet is clearly visible. Comparing this interface for U and P, the downward bend at $x \approx 50$ mm for U starts already at $x \approx 5$ mm for P, in combination with much higher temperatures. The further course of the hot temperature band is qualitatively similar to case U for the upper half of the jet. Unlike case U, the bottom vicinity of the jet also displays high temperatures. Since no direct recirculation could be found here, the pilot flame must encompass the main jet right at the burner base plate and feed hot burned gas all around the jet root. This is particularly visible in view T, where the (outer) pilot flames create hot spots on the lateral sides right at the nozzle rim. However from this information no statement can be drawn about whether there is reaction at the bottom side of the jet. Comparing the bottom and the lateral temperature interfaces (view S and T) to the jet shear layer from the PIV data, the bend of temperature into the jet (i.e. reaction) seems to happen further downstream at $x \approx 50$ mm, which can also be estimated from the OH*-CL images at the bottom side. The temperature boundary layers merge somewhere around $x \approx 150$ mm and no steady cold regions can be found in the second window segment for P.

Although the adiabatic flame temperature based on the global air excess ratio λ_g is 1970 K for case P, which is only slightly higher than U (1900 K), the local adiabatic flame temperature of the pilot burner with $\lambda_p = 1.0$ is 2450 K, which explains the high temperature regions in the proximity of the pilot burner. At the very end of the measurement volume at $x \approx 330$ mm, the average exhaust temperatures for both cases are similar and only differ by less than 100 K. However, the local hot spots in case P lead to a much higher NO_x formation, which can be seen in the results of the exhaust gas analysis in Tab. 2. It is obvious that the pilot burner would not be worthwhile for a real application at this academic operation point, since both NO_x and CO rise with the increase of temperature. See the associated paper A [14] for a realistic turndown investigation.

3.2 3D Reconstruction

One interest of the detailed laser measurements was on the three-dimensional structure of the flame, which is the reason for the chosen high number of measurement planes and different orientations (see Fig. 3). Since the display of all these planes would be confusing, an attempt is made to reconstruct a three-dimensional image from the numerous two-dimensional slices. This reconstruction was done for the averaged PIV data and for the averaged temperature fields.

First, for every averaged measurement plane the information of the first and second window was put together and the gap was filled by interpolation in x-direction. Second, different three-dimensional volumes were interpolated from the two-dimensional information: One volume was created by interpolating in z over the slices of orientation S, one by interpolating in y over the slices of orientation T, and one by interpolating in cylindrical coordinates over all the slices. These three volumes were then again added together, averaged, mirrored in z and smoothed to obtain the final 3D data (this means symmetry in z is enforced here). The data is then visualized by isosurfaces of the respective quantities. Note that the measurement grid is too coarse to actually resolve small scale structures and the plots should be seen as general overview of the large scale flow structures.

Figure 8 shows isosurfaces for the axial velocity v_x. Displayed in blue is the extent of the recirculation zone, i.e. $v_x = 0$ m/s. Green is the interface of $v_x = 40$ m/s and can be seen as the jet boundary. Red is the interface at $v_x = 80$ m/s and

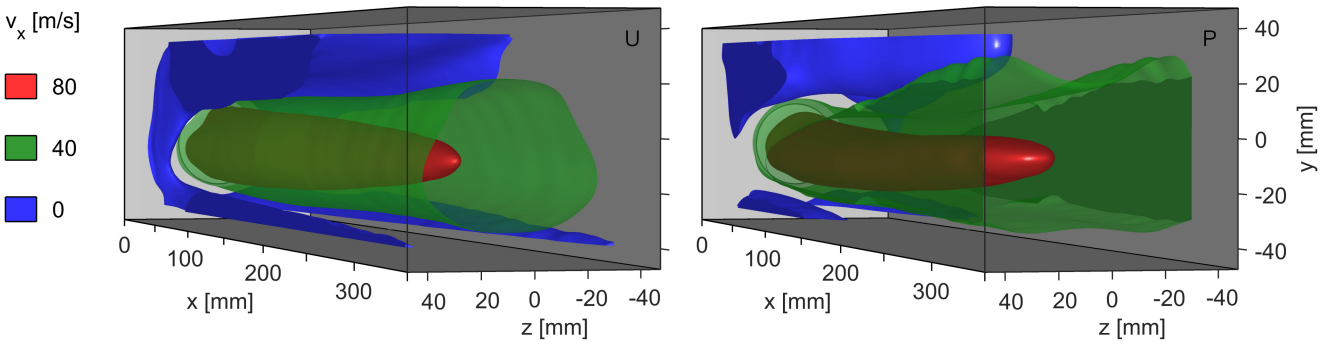

Fig. 8. 3D reconstruction of average PIV data. Shown are isosurfaces of axial velocity.

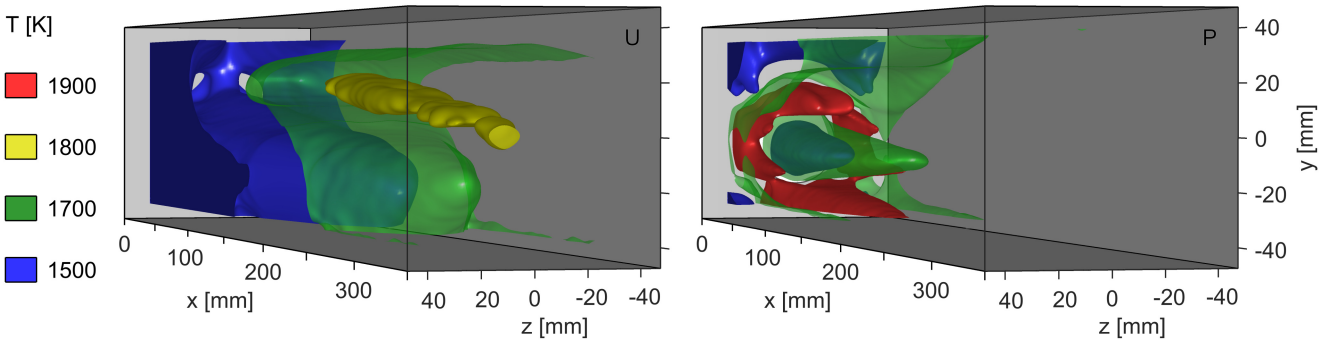

Fig. 9. 3D reconstruction of average temperature data from OH-LIF. Isosurface at 1800 K is omitted for case P.

shows the inner core of the jet. The upper recirculation zone that was seen in the two-dimensional flow fields extends laterally for case U, but is concentrated close to the symmetry plane for P. In the lower edges of the combustor, streaks of reverse flow can be seen, which are more prominent for case U. In addition to these stripes, the recirculation zone encompasses the jet root at the nozzle rim for case U and connects at the bottom side. This effect cannot be seen for case P.

The most striking difference is seen for the green jet boundary. While this shows an expanding round jet for case U, the jet is constricted into a rectangular shape through the pilot burner flow. Further downstream, the jet even becomes concave, which could be the reason for the lumped recirculation zone in this case. The penetration length of the inner jet core is not influenced by the pilot burner flow, the tip of the red surface is almost at the exact same position. However, a slight downward bend is visible for the jet core in case P.

Figure 9 shows the corresponding temperature fields: For case U, cold regions (blue) can be seen in the jet and in the whole front part of the combustor, which qualitatively shows the lift-off of the flame. These cold regions only occur in the jet center close to the inflow for case P as well as in the upper front corner of the combustor. The green interface shows intermediate temperatures and separates the front from the rear part in case U, while it covers almost the complete domain in case P. Note how the intermediate temperatures are drawn into the recirculation zone in case U. Red shows hot regions, that only occur in the pilot flame. It is nicely visible how the pilot flames encompass the jet root and connect at the bottom, where the extent of the hot region is even longer than at the top. Since these hot temperatures do not exist for case U, a second intermediate temperature interface is drawn in yellow, to show the area of maximum temperatures in the center of the combustion chamber.

3.3 Simultaneous Single Shot Analysis

It is known from former studies, that the fluid dynamic and thermochemical processes in a FLOX® combustor are highly turbulent and unsteady. To understand these processes in detail and to reveal the underlying phenomena it is necessary to examine the instantaneous measurements in addition to the statistical analysis. PIV and OH-LIF measurements have been performed simultaneously in addition to the above presented consecutive done measurements, since the quality of the OH-LIF absorption measurements suffers from the PIV particles and the degeneration of window transmittance. That is why for the simultaneous results, only a qualitative OH signal in arbitrary units will be shown and no temperatures could be derived. However, the reader can still think of the shown OH-LIF signal as a qualitative temperature information.

For each case U and P, four instantaneous simultaneous snapshots for orientation S and two for orientation T are shown in Fig. 10. These plots should be convenient for the reader to get a representative impression out of the total 500 single shots

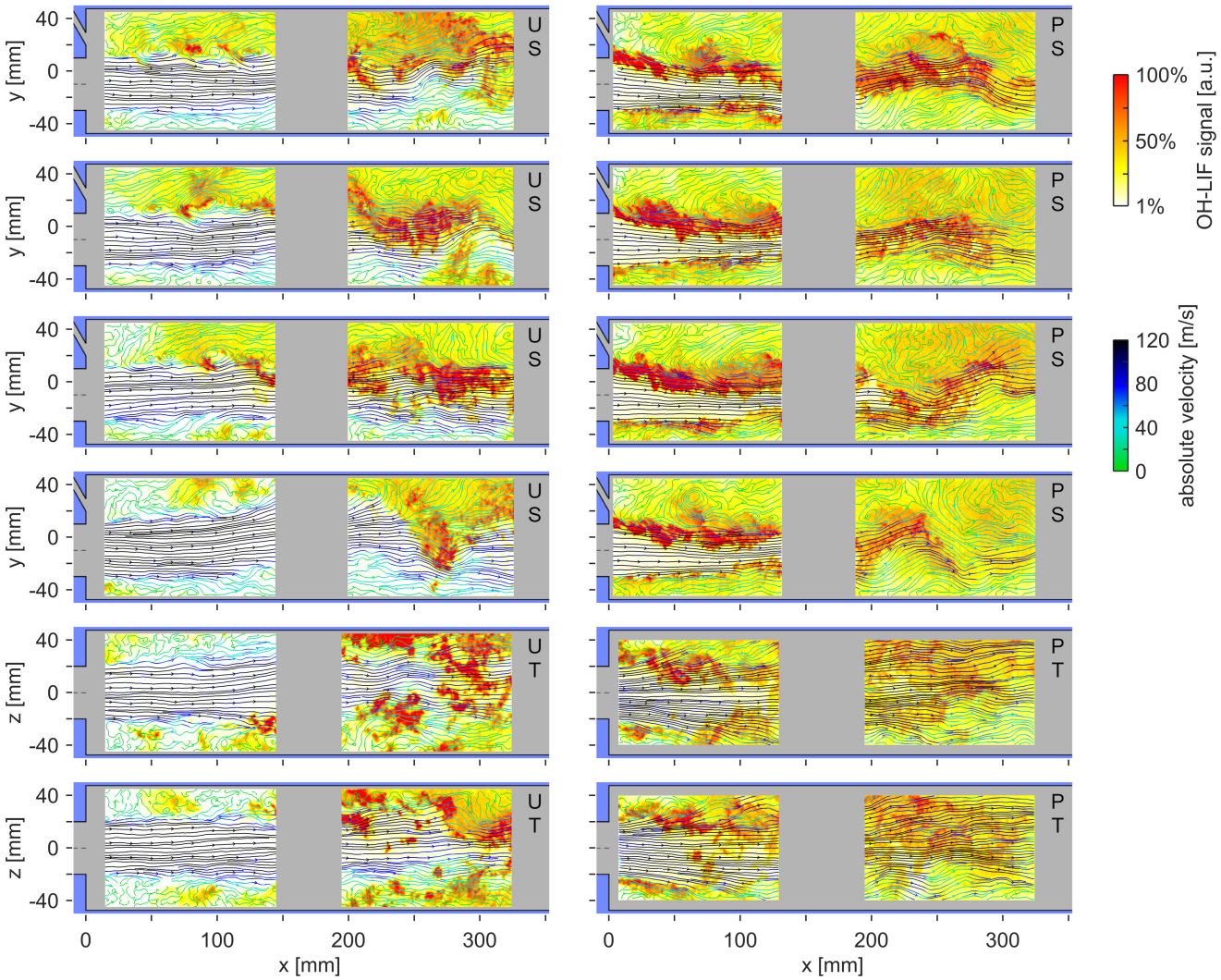

Fig. 10. Simultaneous single shots of OH-LIF and PIV. The respective front and rear single shot are put together arbitrarily. Left images show the unpiloted case U, right images the piloted case P. Top four rows show the sideview S, at different instants of time. Bottom two rows show the topview T, at different instants of time.

per measurement. However the conclusions drawn here are also based on the analysis of all available data.

The highly unsteady turbulent flow field and the disrupted flame fronts are obvious and are typical of a FLOX® combustor. In all shots for orientation S, it is noticeable that the large recirculation zone on the upper side of the jet actually consists of many smaller scale vortices. Especially for case U, it seems these vortices occur in an almost regular pattern in the shear layer between jet and recirculation zone. These vortices both transport burned hot gas (yellow) into the high momentum jet as well as unburned gas outwards into the recirculation zone.

The sporadic hot spots (red) visible in the first window segment contain high amounts of OH, which could either be due to superequilibrium OH (even though it is quickly equilibrated it is present for a short time and detected) or nascent OH from reaction zones that has not suffered a temperature loss (in contrast to the recirculated "old" OH). Together with a steep gradient in OH concentration (white to red) this allows for the interpretation of these hot spots being reacting flame zones and will be referred to as flame kernels in the following.

It is seen that these flame kernels often coincide with the aforementioned vortices. Furthermore, these kernels can typically be seen on the lower left side of the corresponding vortex, where hot burned gas is entrained into the jet core. The opposed side of the vortex, where cold fresh gas is transported into the hot surrounding exhaust gas seems to show less intensive reaction. While the flame kernels can only be seen in low speed regions in the shear layer up to $x \approx 120\,\mathrm{mm}$, burning structures can be seen within the jet core at the rear part of the first window and in the whole second window, at flow velocities of more than 100 m/s. Taking a look at the hot structure at $x = 140\,\mathrm{mm}$ in the third snapshot of U (view S), it seems that once a flame kernel is generated by a vortex introducing hot exhaust gas into the jet (e.g. at $x = 95\,\mathrm{mm}$), this kernel can grow inside the high momentum but low shear region in the jet core (at $x = 140\,\mathrm{mm}$). In the rear window at $x > 200\,\mathrm{mm}$

actually most of the reaction takes place within these high momentum regions. On the bottom side of the jet small scale vortices can be seen but are not as pronounced as in the upper shear layer. In contrast to the averaged OH-LIF information, hot regions can be seen every now and then at the bottom side of the jet (even at $x = 10$ in the fourth snapshot), but they never seem to initiate reaction with the fresh gas. One reason could be that the small scale vortices and the hot gas pockets are washed away too quickly, since there are no zero velocity zones like in the upper recirculation zone.

In contrast, for case P hot burning regions inside the jet core can be seen right from the start at the upper side of the jet and grow towards the jet axis further downstream. Here the small scale vortices at the upper side of the jet seem to have no influence on flame stabilization. Furthermore there are no single flame kernels, but rather a connected flame front. Obviously, the hot reacting fluid from the pilot flame penetrates the incoming jet and causes a continuous ignition of the fresh gas right at the jet root. This looks different on the bottom side of the jet: Here the interface of hot and cold gas follows the jet boundary up to $x = 70 - 80$ mm, and neither vortices nor the pilot flow can be seen to penetrate the jet.

Having a close look at the flame front in case P, many small scale wrinkles can been seen which indicate highly turbulent combustion in the high Reynolds number flow. The PIV resolution is too coarse to resolve scales in this order of magnitude.

In view T for case U, the lateral sides of the jet seem to show a similar behavior as the bottom side in the first window: No pronounced vortices can be seen, and the sporadic hot gas regions do not seem to interact with the jet flow. In the second window, a disrupted pattern of fresh and burned gas can be seen, which shows that reacting fluid elements are distributed over a large volume. This again is a a typical feature of the highly turbulent combustion in a FLOX® combustor.

For view T of case P, this disrupted pattern is rather seen in the first window, while in the second window almost no unreacted gas (white zones) can be found. This statement also holds for the other plots: The visual impression always looks similar for the first window of case P and the second window of case U. This supports the statement that the pilot burner accelerates the process that is otherwise performed by self-sustained vortices further downstream.

4 Conclusions and Outlook

Two cases of a high momentum jet flame at elevated pressure have been analyzed by laser measurement techniques. The results show a similar flow field with a large recirculation zone, but a lifted flame for the operation without pilot (U) and an attached and shorter flame for the piloted case (P). The simultaneous single shot analysis suggests, that the flame for case U is stabilized by small vortices in the shear layer between jet and recirculation zone, which penetrate the jet with hot burned gas and initiate flame kernels. These kernels could be seen to grow in the jet core region once they pierce the shear layer. The appearance of single flame kernels give rise to the idea of a process based on auto-ignition. However, their temporal development could not be resolved by the low-speed measurement setup.

The single shots of case P led to the conclusion of the pilot burner acting like the vortices in case U, feeding hot reacting gas into the jet core. Since the pilot burner is impinging the jet in a steady manner, a permanently burning flame front is found in this case rather than distinct flame kernels. This does not imply a flame stabilization mechanism based on flame propagation, since the pilot burner is most likely permanently igniting the incoming main jet.

Evaluation of the presented data is ongoing. An attempt will be made to estimate temperatures for the simultaneous single shot measurements, based on a comparison of the averaged OH concentration. The assumptions drawn from the single shot results will be verified in a statistical correlation.

Additional laser Raman measurements have been performed on the same reference flames and will be published soon. These can be used to verify the temperatures presented in this work and to gain insight into the thermochemical structure in the shear layer. Furthermore, Coherent Anti-Stokes Raman Spectroscopy (CARS) measurements are planned on this burner for the near future.

In order to track the temporal development of the flame kernels seen in case U, simultaneous high-speed laser measurements are desired and will be performed in the future. These measurements will be done in a simplified lab setup, since the pulse energies of the high-speed lasers are to small to obtain a sufficient signal to noise ratio at the harsh conditions at the test rig.

Acknowledgements

The investigations were conducted as part of the joint research program CEC (Siemens Clean Energy Center). The work was supported by the Bundesministerium für Wirtschaft und Energie (BMWi) as per resolution of the German Federal Parliament under Grant No. 03ET7011D. The authors gratefully acknowledge Siemens AG Energy Sector for their support to publish this paper.

The authors would like to thank S. Peukert and T. Schiek for the installation as well as R. Schieferstein for the test rig operation.

References

[1] FLOX® is a registered trademark of WS Wärmeprozesstechnik GmbH, Renningen, Germany.

[2] Wünning, J. A., and Wünning, J. G., 1992. "Burners for Flameless Oxidation with Low NO_x Formation even at Maximum Air Preheat". *Gaswärme International,* **41**(10), pp. 438 – 444.

[3] Lückerath, R., Meier, W., and Aigner, M., 2007. "FLOX® Combustion at High Pressure with Different Fuel Compositions". *Journal of Engineering for Gas Turbines and Power,* **130**(1), pp. 011505–1 – 011505–7.

[4] Lammel, O., Schütz, H., Schmitz, G., Lückerath, R., Stöhr, M., Noll, B., Aigner, M., Hase, M., and Krebs, W., 2010. "FLOX® Combustion at High Power Density and High Flame Temperatures". *Journal of Engineering for Gas Turbines and Power,* **132**(12), p. 121503ff.

[5] Danon, B., de Jong, W., and Roekaerts, D. J. E. M., 2010. "Experimental and Numerical Investigation of a FLOX Combustor Firing Low Calorific Value Gases". *Combust. Sci. Technol.,* **182**(9), pp. 1261 – 1278.

[6] Rödiger, T., Lammel, O., Aigner, M., Beck, C., and Krebs, W., 2013. "Part-Load Operation of a Piloted FLOX® Combustion System". *Journal of Engineering for Gas Turbines and Power,* **135**(3), pp. 031503–1.

[7] Lammel, O., Rödiger, T., and Severin, M., 2014. "Industriegasturbinenbrenner für alternative Brenngase". *Project Report. DOI: 10.2314 / GBV:817024255*.

[8] Lammel, O., Rödiger, T., Stöhr, M., Ax, H., Kutne, P., Severin, M., Griebel, P., and Aigner, M., 2014. "Investigation of Flame Stabilization in a High-Pressure Multi-Jet Combustor by Laser Measurement Techniques". *ASME Paper no. GT2014-26376*.

[9] Coelho, P., and Peters, N., 2001. "Numerical Simulation of a Mild Combustion Burner". *Combustion and Flame,* **124**, pp. 503 – 518.

[10] Schütz, H., Lückerath, R., Noll, B., and Aigner, M., 2007. "Complex Chemistry Simulation of FLOX®: Flameless Oxidiation Combustion". *Clean Air International Journal on Energy for a Clean Environment,* **8**(3), p. 239ff.

[11] Lammel, O., Stöhr, M., Kutne, P., Dem, C., Meier, W., and Aigner, M., 2012. "Experimental Analysis of Confined Jet Flames by Laser Measurement Techniques". *Journal of Engineering for Gas Turbines and Power,* **134**(4), pp. 041506–1.

[12] Yin, Z., Nau, P., Boxx, I., and Meier, W., 2015. "Characterization of a Single-Nozzle FLOX Model Combustor Using KHz Laser Diagnostics". *ASME Paper no. GT2015-43282*.

[13] Di Domenico, M., Gerlinger, P., and Noll, B., 2011. "Numerical Simulations of Confined, Turbulent, Lean, Premixed Flames Using A Detailed Chemistry Combustion Model". *ASME paper no. GT2011-45520*.

[14] Lammel, O., Severin, M., Ax, H., Lückerath, R., Tomasello, A., Emmi, Y., Noll, B., Aigner, M., and Panek, L., 2017. "High Momentum Jet Flames at Elevated Pressure, A: Experimental and Numerical Investigation for Different Fuels". *ASME Paper no. GT2017-64615*.

[15] Dandy, D. S., and Vosen, S. R., 1992. "Numerical and Experimental Studies of Hydroxyl Radical Chemoluminescence in Methane Air Flames". *Combust. Sci. Technol.,* **82**, pp. 131 – 150.

[16] Heinze, J., Meier, U., Behrendt, T., Willert, C., Geigle, K.-P., Lammel, O., and Lückerath, R., 2011. "PLIF Thermometry Based on Measurements of Absolute Concentrations of the OH Radical". *International journal of research in physical chemistry and chemical physics,* **225**(11-12), pp. 1315 – 1341.

[17] Coxon, J., 1980. "Optimum molecular constants and term values for the $X^2\Pi(v \leq 5)$ and $A^2\Sigma^+(v \leq 3)$ states of OH". *Can. J. Phys.,* **58**(933).

[18] Rahmann, U., Kreutner, W., and Kohse-Höinghaus, K., 1999. "Rate-equation modeling of single and multiple quantum vibrational energy transfer of OH ($A^2\Sigma^+, v' = 0$ to 3)". *Applied Physics B,* **69**, pp. 61 – 70.